Available online at www.sciencedirect.com
ScienceDirect
Journal of Magnetic Resonance 182 (2006) 106–114
JMR Journal of Magnetic Resonance
www.elsevier.com/locate/jmr

Theory of MRI in the presence of zero to low magnetic fields and tensor imaging field gradients

C.A. Meriles [a,*], D. Sakellariou [b], A.H. Trabesinger [c]

[a] Department of Physics, City College of New York—CUNY, New York, NY 10031, USA
[b] DSM/DRECAM/Service de Chimie Moléculaire, CEA Saclay, 91191 Gif-sur-Yvette Cedex, France
[c] 110 Stapleton Hall Road, London N4 4QA, UK

Received 15 April 2006; revised 15 June 2006
Available online 7 July 2006

Abstract

Today, all commonly practiced magnetic resonance imaging (MRI) reconstruction methods assume that the magnetic field created by the gradient coils is everywhere truncated by a dominant static uniform magnetic field. However, with the advent of SQUID detected MRI at microtesla fields, the opposite limit attracts attention, i.e., image formation in the unperturbed tensor field of the gradient coils. Here, we show by numerical simulations that, in principle, it is possible to reconstruct the image of an object in the absence of a uniform static field, working with the same gradient field setup as used in conventional MRI. Our calculations show that this approach could increase the image resolution limit attainable at low fields with a minimal incorporation of additional hardware and pulse sequences.

Keywords: Low-field MRI; Concomitant field gradient

1. Introduction

Magnetic resonance imaging (MRI) is based on the use of inhomogeneous or 'gradient' fields supplementing on an otherwise uniform and time invariant magnetic field. These additional fields are created by 'gradient coils' designed to alter the magnetic field *amplitude* along a pre-selected direction without changing the *direction* of the total field. The result is a relation between the resonance frequency and the spatial location, which—ultimately—makes it possible to reconstruct the image of the object [1].

From the viewpoint of classical electrodynamics, this scheme may seem, at first sight, not feasible. In the absence of free currents, Maxwell's equations predict that everywhere in space the curl and the divergence of a magnetic field must vanish. Therefore, regardless of the geometry and position of the gradient coils, it is impossible to generate a magnetic field that locally only changes its amplitude without also altering its direction. Of course, the field of a 'gradient coil' indeed has not only components parallel to the uniform field, but also such perpendicular to it. The latter are sometimes referred to as 'concomitant gradients' [2,3]. However, if the amplitude of the uniform field is much larger than any component of the total field created by the gradient coils (which is described by a tensor), the non-secular components become negligible to first order in the description of the spin evolution. These non-secular components are of course exactly the concomitant gradients. In the general case, obviously, they must be taken into account.

Traditionally, there has been a drive to uniform magnetic fields as intense as technically possible because the amplitude of the resonance signal grows nearly quadratically with the field intensity. During the last years, however, several research groups have explored an inverse path in which, systematically, the field amplitude is reduced. As a matter of fact, there are several reasons that justify this tendency [4]. In the first place, image distortions due to local changes of the sample susceptibility—very common in biological samples—disappear

* Corresponding author. Fax: +1 212 650 7948.
E-mail address: cmeriles@sci.ccny.cuny.edu (C.A. Meriles).

1090-7807/$ - see front matter © 2006 Elsevier Inc. All rights reserved.
doi:10.1016/j.jmr.2006.06.018

linearly with decreasing field. Further, the reduction of the irradiation frequency accompanying the smaller fields makes it possible, e.g., to image the content of metal-shielded systems, which, otherwise, would remain invisible at higher frequencies. Finally, practical considerations make low-field MRI particularly attractive: for example, the inherent simplicity of low-field electro-magnets could lead to portable imaging systems or devices with wide-open geometry in addition to reducing associated costs. This has been shown by Macovski and collaborators who employed pre-polarization methods in relatively inhomogeneous fields to obtain images for medical use [5,6]. In the same direction, hyperpolarized xenon-129 and helium-3 MRI has been demonstrated by several groups [7,8] at fields that do not demand superconducting magnets and quite recently has been applied to image human lungs [9,10].

In particular during the last decade, the use of Superconductive Quantum Interference Devices (SQUIDs) has led the way to field detection at nearly arbitrarily low frequencies. For example, it has been shown that it is possible to carry out high-resolution NMR spectroscopy in fields as low as 5×10^{-2} gauss [11,12] and, more recently, the SQUID has also been used to obtain magnetic resonance images in fields of only 1 gauss [13–16]. Here, we explore the theory of schemes aimed at reconstructing images in the limit where the static field does not truncate the transverse components of a field generated by a gradient coil. (For brevity's sake, we will use from now on the term 'gradient field' to indicate the total magnetic field created by a gradient coil.) Implicitly, we assume that a SQUID is used for signal acquisition, but other detection schemes (e.g., atomic magnetometers [17]) could be used equivalently. Two different approaches are discussed, both of them utilizing the fact that the rotation symmetry of a curl-free field can be broken by means of r.f. irradiation and/or pre-polarization in a homogeneous field. The first ansatz is based on temporal averaging of undesired gradient field components such that an average Hamiltonian can be formulated that only contains fields in one spatial direction [18]. In the second scheme, we encode the initially missing information into Fourier coefficients and devise a protocol that allows us to determine these coefficients.

In both cases, our images will be the result of numerical simulations. However, we will always indicate the underlying physical array and we will also discuss some issues related to the practical implementation of the schemes. For simplicity, we will concentrate here on the case of Golay gradient coils [19] and we will restrict our analysis to two dimensions. However, it will soon become apparent that both methods could be extended to three dimensions if necessary. An approach resembling the first scheme has been used in the past to render planar a radial radio-frequency field gradient. This scheme has been used in the context of radio-frequency-gradient spectroscopy to select specific coherence pathways [20,21].

2. Scheme 1

Consider the (fictive) setup depicted in Fig. 1. A Golay coil equivalent to those used in a standard imaging device generates a static non-uniform magnetic field. The system has three mutually orthogonal solenoids that create intense and uniform magnetic pulses along any desired direction (not shown). For simplicity, we will assume here that our sample is thin—i.e., expansion along one dimension is negligible—and that it is contained in the shaded region in the center of the array. Nearby, a coil coupled, e.g., to a SQUID picks up the signal of the precessing nuclear magnetization. A pre-polarization solenoid (not shown) completes the setup. In this case, we will assume that it is oriented perpendicular to the sample plane although, in general, this is not necessary. Notice that, with the exception of this last coil (inherent to pre-polarization based systems), the number of coils used is the same as in a high-field imaging system.

The magnetic field due to the saddle coil at each point (x,z) in the sample region can be described by the relation

$$\vec{\mathbf{B}}(x,z) = g(z\hat{\mathbf{x}} + x\hat{\mathbf{z}}), \tag{1}$$

where g indicates the (constant) amplitude of the gradient field. This is readily derived from the condition that curl $(\vec{B}) = 0$ and the fact that the gradient coil is designed in a way to create a linear gradient $\frac{\partial B_z}{\partial x} = g = \text{const}$. Fig. 2A shows the resulting field. The magnitude of the field increases linearly with the distance r to the center of the setup. Along a ring of fixed radius, its direction varies linearly with the angle.

The Hamiltonian of an uncoupled spin in the presence of this magnetic field writes

$$H = \gamma\vec{\mathbf{B}}\cdot\vec{\mathbf{I}} = \omega_{\mathrm{r}}(I_x\sin\theta + I_z\cos\theta), \tag{2}$$

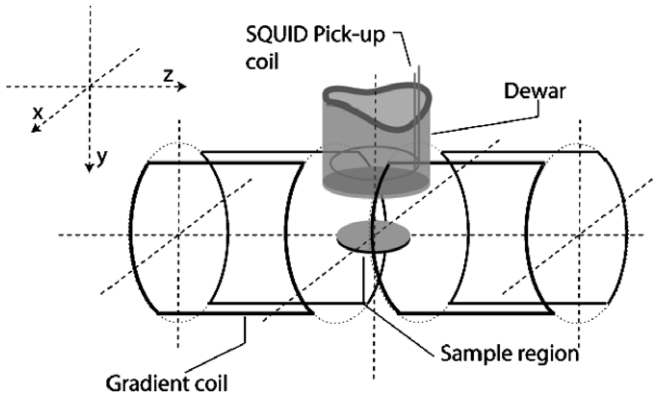

Fig. 1. Sketch of our virtual setup. The main magnetic field is created by a saddle coil. The sample, located in the shaded central region, is assumed to be thin compared to the dimension of the saddle coil perpendicular to the sample plane (in this way, field components perpendicular to the sample can be safely neglected). Detection is carried out along the y-axis by a pick-up coil (gradiometer configuration) inductively coupled to a SQUID. Spin evolution is manipulated by dc-field pulses due to three orthogonal Helmholtz coils surrounding the sample. A pre-polarization coil is also used to create an initial spin alignment along any desired direction. For simplicity, neither of these last coils has been displayed in the picture.

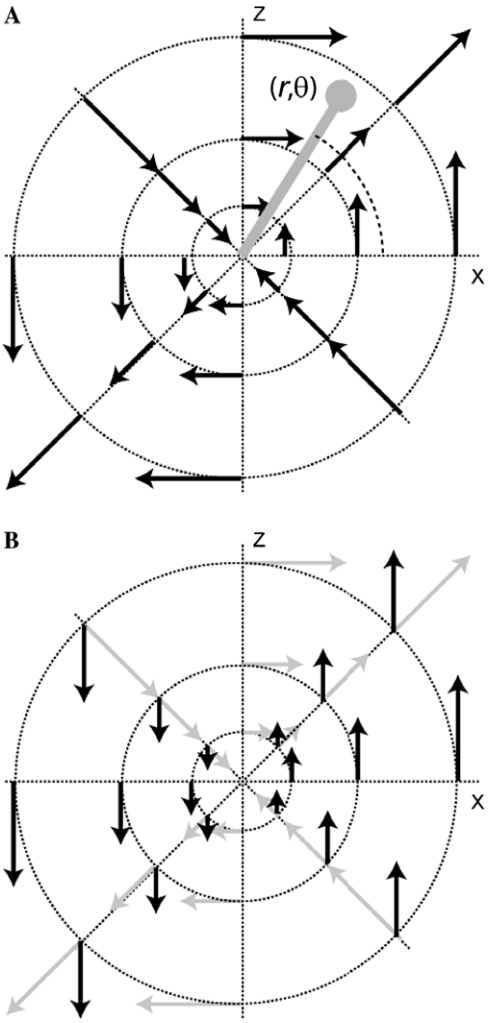

Fig. 2. (A) Magnetic field geometry in the sample region. The field magnitude is zero at the center and increases linearly with the radius. Along a given ring, the change in the field direction is proportional to the angle. (B) Black arrows now indicate direction and magnitude of a virtual "average field" resulting from the superposition of the original magnetic field (gray arrows) and a second one in which, at all sites, the component along the x-axis has changed sign (reflection about the z-axis). The resulting field points along the z-axis and its magnitude changes linearly along x. Although a field like this one is not physically achievable, this will be the field experienced "on average" by the spin system if a train of π-rotation pulses is applied during the evolution (see text).

where $\omega_r = \gamma g\sqrt{x^2+z^2}$, $\tan\theta = z/x$ and γ denotes the gyromagnetic ratio. Formula (2) implies that the resonance frequency only depends on the radial distance to the center of the array, i.e., the frequency spectrum only contains information about the distance from the center, but no angular resolution.

This lack of information can be overcome by eliminating one of the vectorial components in (1); the resulting magnetic field varies linearly over the sample without altering its direction (exactly as in the presence of a truncating field). As shown in Fig. 2B, this is the situation if we superimpose at each point in space two magnetic fields: the original one and another that we will call reflected field, obtained at each point after a reflection on an axis, for example, the z-axis. In Fig. 2B, the resulting field points along the z-axis and its magnitude changes linearly with x. This operation has rendered Cartesian the original cylindrical symmetry and, in principle, allows us to obtain a one-dimensional image of the object, in this case, perpendicular to the reflection axis.

Such 'reflected fields', however, are not curl-free and therewith not physical. But it is possible to induce the effect of reflection if π pulses along a pre-selected axis are applied during the spin evolution. The formal description of this idea follows below. Let us consider the scheme of Fig. 3. The initial preparation of the system is followed by a train of short and intense π rotation pulses along the direction $\hat{\mathbf{x}}'$, separated by a time τ. If the acquisition is done stroboscopically following every other π pulse (see figure), the evolution operator U evaluated at the n-th cycle satisfies the relation

$$U(2n\tau) = [U(2\tau)]^n, \tag{3}$$

where

$$U(2\tau) = \exp(-iH\tau)\exp(-i\pi I_{x'})\exp(-iH\tau)\exp(-i\pi I_{x'}). \tag{4}$$

Explicitly rewriting the Hamiltonian and using the Magnus expansion, we get

$$\begin{aligned} U(2\tau) &= \exp\left(-i\gamma\tau(B_{x'}I_{x'} + B_{z'}I_{z'})\right)\exp(-i\gamma\tau(B_{x'}I_{x'} - B_{z'}I_{z'})) \\ &= \exp(-i2\gamma\tau\vec{\mathbf{B}}_{\text{eff}}\cdot\vec{\mathbf{I}}) \end{aligned} \tag{5}$$

where [22,23]

$$\vec{\mathbf{B}}_{\text{eff}}\cdot\vec{\mathbf{I}} = B_{x'}I_{x'} + \frac{\gamma\tau}{2}B_{z'}B_{x'}I_Y + O(\tau^2). \tag{6}$$

Notice that, as deduced from Eq. (5), the result of applying π pulses can be interpreted as a "reflection" of the field component perpendicular to the pulse direction during half of the evolution interval. When the inter-pulse spacing is much smaller than the inverse of the maximum frequency created by the gradient coil, the effective value of the field converges to the desired average (first term in the series of Eq. (6)). As expected, the average field points along the direction of the pulses. To find out the direction of the gradient, we rewrite $B_{x'}$ in the unprimed reference frame. It is simple to show that

$$B_{x'} = B_x\cos\theta + B_z\sin\theta = g(z\sin\gamma + x\cos\gamma), \tag{7}$$

with $\gamma = \frac{\pi}{2} - \theta$. Thus, the effective field magnitude is given by

$$\vec{\mathbf{B}}_{\text{eff}}\cdot\vec{\mathbf{I}} = \vec{\mathbf{g}}_{\text{eff}}\cdot\vec{\mathbf{x}}I_{x'} + O(\tau), \tag{8}$$

where $\vec{\mathbf{g}}_{\text{eff}} = g(\cos\gamma, \sin\gamma)$ and $\vec{\mathbf{x}} = (x, z)$. This result implies that when the train of uniform field pulses is applied along a direction $\hat{\mathbf{x}}' = (\cos\theta, \sin\theta)$, the effective field gradient $\vec{\mathbf{g}}_{\text{eff}}$—and, thereby, the projection axis of the image—points along a direction $\hat{\mathbf{x}}'' = (\cos\gamma, \sin\gamma)$. Thus, this method is

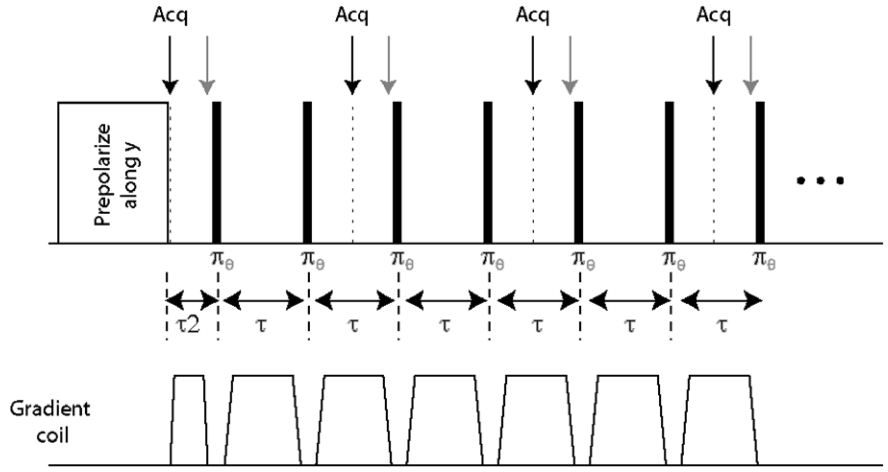

Fig. 3. Pulse sequence in Scheme 1. The system is initially pre-polarized along the y-axis. A train of π-rotation dc-field pulses along a direction θ manipulates further evolution in the gradient field. The pulse repetition rate should be fast compared to the maximum local Larmor frequency in the gradient field. Acquisition is performed stroboscopically in between pulses. Different acquisition schemes (indicated by black or grey arrows) are possible: acquisition at the midpoint of the interval (black ink) symmetrizes the cycle canceling out all odd terms in the average Hamiltonian expansion. Acquisition at the end of the interval (gray ink) is appropriate for a longer detector dead time.

equivalent to projection/reconstruction with the exception that in the present case the change in the gradient direction is accompanied by a simultaneous change in the direction of the (effective) field.

Fig. 4 shows that, given the right set of parameters, this procedure yields a faithful representation of an object (Fig. 4B). The geometry chosen was that shown in the figure inset with spins distributed on a Cartesian grid with 128×128 points. The simulation assumes a constant field gradient of maximum amplitude 0.08 gauss. The pulse amplitude was set to 3 gauss and the spacing to 0.5 ms. The sample relaxation time was taken to be 1 s and, due to the relatively short inter-pulse spacing, effects due to self-diffusion were neglected. In correspondence with the pre-polarization pulse used in Ref. [12], we assumed that the spins were initially aligned in a direction perpendicular to the figure plane.

Fig. 4B shows the result of a numerical simulation obtained after 128 projections and a standard processing. The figure correctly reproduces the spatial density of the spin system, but it is clear that some artifacts appear as the distance to the center increases. This effect is intrinsic to the method of projection/reconstruction (cf. Fig. 4A, where a simulation of the high-field case is shown). In the present case, however, the problem becomes more acute because the correction terms in Eq. (6) are more important in the outer regions of the sample. In this respect it is worth mentioning that the degree to which Eq. (8) correctly represents the effective Hamiltonian improves considerably if the acquisition is made at half the inter-pulse interval and not at the end (Fig. 4C). This is because the repeating unit during the system evolution becomes symmetric and, as a consequence, all odd terms of the Magnus expansion become zero [22] (see Eqs. (5) and (6)). Such a scheme is obviously advantageous as long as the inter-pulse and acquisition intervals are compatible with the detection dead time. We will come back to this and other practical issues in the final section of the manuscript.

This scheme naturally extends to the case in which a 'background' homogeneous, time-independent magnetic field adds to the field created by the gradient coil. This is due to the fact that the component of the background field parallel to the direction of the pulses will not be removed from the evolution and will simply translate into a frequency shift of the image projection; this shift, of course, varies with the direction chosen for the dc-field pulses (and scales with the projection of the background field along the pulsing direction). The result of simulations for background fields of different relative magnitudes are shown in Fig. 5. For a fixed inter-pulse interval τ, Scheme 1 fails as the background field becomes comparable or larger than the gradient field (because of increasingly imperfect averaging). This behavior is reminiscent of that found in standard MRI in the opposite limit although, unlike in this latter case, distortions can be partially mitigated (and eventually, effectively eliminated) at the expense of a shorter τ.

3. Scheme 2

To introduce the idea underlying this method, let us start by describing the free evolution of an uncoupled spin in the gradient field after a pre-polarization pulse. After a time t, the density matrix of the system is given by the relation

$$\rho(t) = U(t)\rho(t=0)U(t)^{-1}, \tag{9}$$

where $U(t) = \exp(-it\gamma\vec{\mathbf{B}}\cdot\vec{\mathbf{I}})$ is the system evolution operator. Assuming that the pre-polarization pulse is applied along the y-axis, the density matrix is (disregarding proportionality constants) $\rho(0) = I_y$. Inserting this into Eq. (9), it follows that

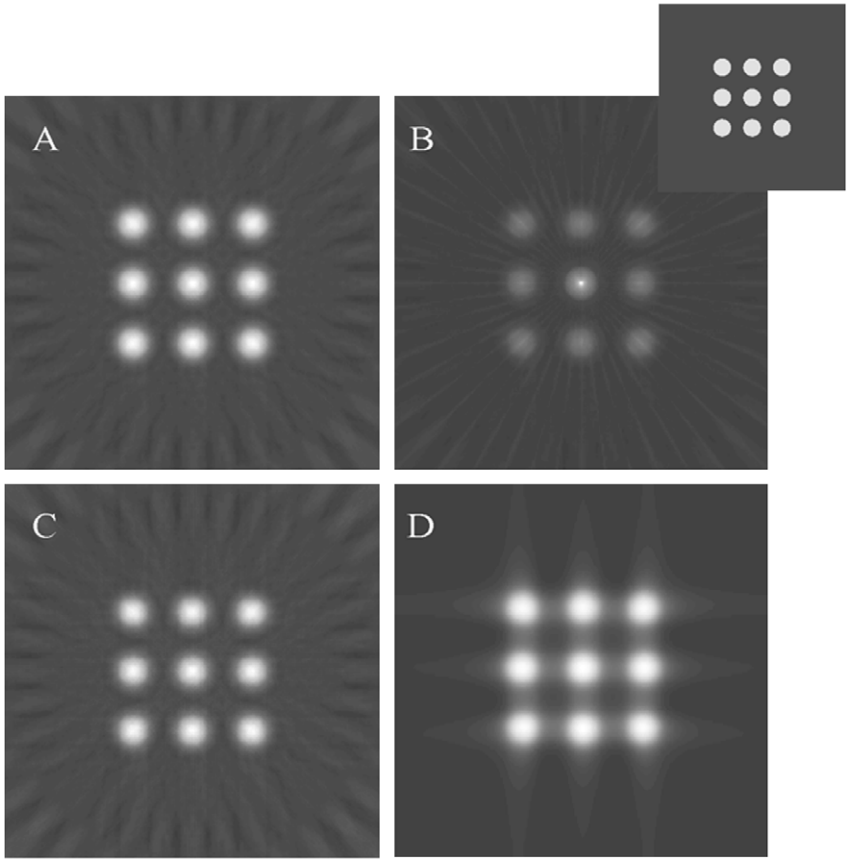

Fig. 4. Comparison of a (virtual) spin distribution (inset) and its image. 0.5 cm diameter disks were evenly spread on a 1 cm square grid (A) standard projection/reconstruction in the presence of a strong and homogeneous magnetic field. The concomitant gradient is truncated. Notice, however, the typical star-like behavior at large radii. (B) Tensor field imaging using Scheme 1 with acquisition at the end of the inter-pulse interval. The sharp peak at the center (zero frequency) is due to imperfect averaging. (C) Same as in (B) but with acquisition at half the inter-pulse interval (see Fig. 3). (D) 2D Fourier reconstruction obtained by a 90-degree change of the pulsing direction at a variable point in the train of Fig. 3. For (B–D), the gradient strength g was 0.12 gauss/cm (500 Hz/cm), the dwell time was 1 ms and the FID had 256 points. Twenty-five equally spaced angles were used covering the range of 0–180. Pulses had an amplitude of 3 gauss.

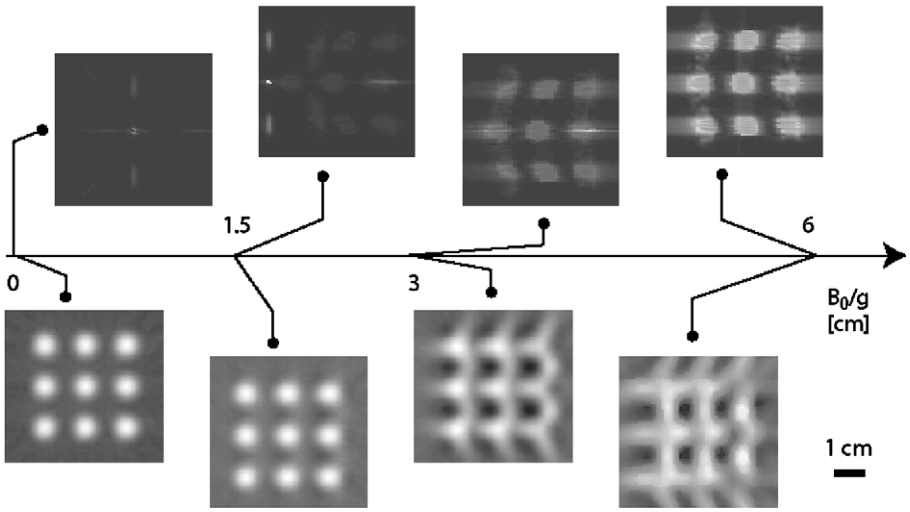

Fig. 5. Upper row: standard MRI in the presence of a uniform magnetic field of decreasing relative amplitude (and therefore decreasing fidelity). From right to left, B_0/g is equal to 6, 3, 1.5, and 0 cm, respectively. Lower row: image reconstruction using the scheme of Fig. 3 and conditions of Fig. 4C in the presence of the same background fields as in (A). Now, however, the fidelity increases with decreasing magnitude of B_0/g. The scale on the lower left corresponds to the separation between centers of closest disks, 1 cm.

$$\rho(t) = I_y \cos(\omega_r t) - I_x \cos\theta \sin(\omega_r t) + I_z \sin\theta \sin(\omega_r t). \tag{10}$$

If detection is done along the y-axis, the resulting signal is

$$S_y(k_r) = \int_0^\infty \mathrm{d}r \cos(k_r r) s_y(r), \tag{11}$$

where $s_y(r) \equiv r\int_0^{2\pi} \mathrm{d}\theta n(r,\theta)$ is the spin density expressed as a function of the cylindrical coordinates r and θ and $k_r \equiv gt$ is the wave vector. Notice that in Eq. (11), the angular dependence of the spin distribution becomes masked because $s_y(r)$ describes only the projection of this distribution on a ring of radius r.

When the pre-polarization is carried out along the x-axis, the induced signal (along y) will be

$$S_x(k_r) = \int_0^\infty \mathrm{d}r \sin(k_r r) s_x(r). \tag{12}$$

In this case, $s_x(r) = \int_0^{2\pi} \mathrm{d}\theta r n(r,\theta)\cos\theta$ indicating that the projection along each ring has now been modulated by the cosine of the angle (or the sine, had the system been pre-polarized along z).

The expressions above can be cast in a general formalism if we notice that, in cylindrical coordinates, the spin density is a periodic function of the angle; $n(r,\theta) = n(r,\theta + 2m\pi)$ for m integer. Hence, we can express $n(r,\theta)$ as

$$n(r,\theta) = \frac{1}{2\pi}\sum_{-\infty}^{\infty} c_m(r) \mathrm{e}^{im\theta}, \tag{13}$$

with $c_m(r) = \int_0^{2\pi} \mathrm{d}\theta r n(r,\theta)\mathrm{e}^{-im\theta}$. Since, by definition, $n(r,\theta)$ is real, $c_{-m} = c_m^*$. It is then not difficult to observe that the projections in formulas (9) and (10) are related in a simple way to the $m = 0, \pm 1$ coefficients of the series (13). Thus, the key point in this scheme turns out to be the fact that we can determine the rest of the coefficients in Eq. (13) if the initial state of the spin system is properly chosen. There are several ways to do this; among them we will briefly describe one below.

Let us consider, for example, two experiments: in both cases, the spins are pre-polarized along the y-axis and evolve freely during an interval $\tau/2$. At the end of this interval, a π pulse is applied, in the first case, along the x-axis (Fig. 6). A straightforward calculation shows that—after a further interval $\tau/2$—the signal in this case will be

$$S_y'(k_r) = -\frac{1}{2}\int_0^\infty \mathrm{d}r \cos(k_r r)\left(c_0(r) + \frac{1}{2}c_{-2}(r) + \frac{1}{2}c_2(r)\right). \tag{14}$$

If, however, the pulse is applied along the diagonal on the xz-plane, the signal will be

$$S_y''(k_r) = -\frac{1}{2}\int_0^\infty \mathrm{d}r \cos(k_r r)\left(c_0(r) + \frac{1}{2i}c_{-2}(r) - \frac{1}{2i}c_2(r)\right). \tag{15}$$

Clearly, both the real and the imaginary components of $c_2(r)$ can be determined by combining the above expressions. If, in a next step, the system is initially prepared along any other direction in the xz-plane, a corresponding set of experiments can be used to determine coefficient $c_3(r)$.

Expressions (14) and (15) can be rewritten in a more compact way if we (arbitrarily) define $c_m(-r) = (-1)^m c_m(r)$. In this case, we have

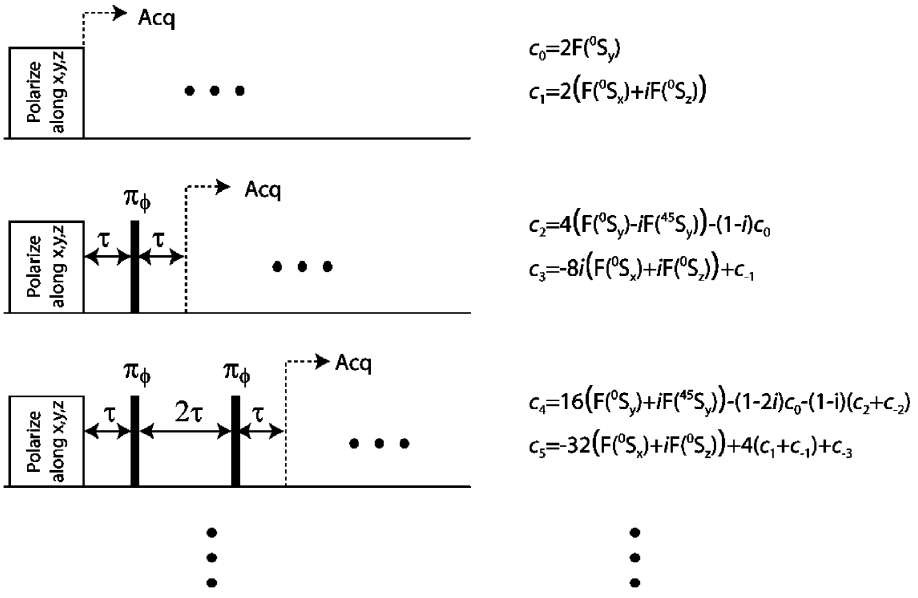

Fig. 6. Pulse sequence and expressions for the first few coefficients of the Fourier series (Formula (13), $m = 0, \pm 1, \cdots, \pm 5$). In Scheme 2, the sample is initially polarized along a given direction and a series of preparation pulses is then applied. Detection is carried out on the first echo following the string of pulses (see text). With each new pulse, four new coefficients in Formula (13) can be determined as a function of the signal Fourier transform and previous coefficients in the series. The expression for each of these coefficients has been listed on the right. Notice that $c_{-m}(r) = c_m^*(r)$.

$$S'_y(k_r) = -\frac{1}{2}\left(\frac{1}{2}F^{-1}(c_0) + \frac{1}{4}F^{-1}(c_2^*) + \frac{1}{4}F^{-1}(c_2)\right),$$
$$S''_y(k_r) = -\frac{1}{2}\left(\frac{1}{2}F^{-1}(c_0) + \frac{1}{4i}F^{-1}(c_2^*) - \frac{1}{4i}F^{-1}(c_2)\right), \quad (16)$$

where $F^{-1}(c_m) \equiv \int_{-\infty}^{\infty} \mathrm{d}r\, e^{ik_r r} c_m(r)$ is the inverse Fourier transform of coefficient $c_m(r)$.

When several π-pulses are used to prepare the initial state (for $m \geqslant 4$), the situation becomes more complex because, in general, several echoes form during the acquisition period. A detailed analysis reveals that all of them contain the same information: the same coefficients can be obtained by individually analyzing any of them. If the inter-pulse separation τ is chosen longer than the inverse of the maximum resonance frequency in the sample, the echoes become well-resolved in time and we can limit our acquisition to, for example, only the first one in the string. With these conditions, we provide in Fig. 6 the expressions for a few low order coefficients obtained after different preparation pulse sequences. With each new pulse in the sequence it is possible to determine two new coefficients in the series as a function of the Fourier transform of the measured signal and previous coefficients. With the exception of $c_0(r)$ (which is real), two experiments are necessary to completely determine each coefficient. Nonetheless, one can show that this number becomes one if two mutually orthogonal pick-up coils are used during detection.

Fig. 7 shows an image of a grid with a model spin distribution after determining 25 coefficients in the Fourier series ($m = 0, \pm 1, \cdots, \pm 12$). Notice that, even though the phantom structure is extremely simple, the absence of cylindrical symmetry and the sharp edges in the original spin distribution bring into evidence most of the features intrinsic to this method. According to formula (13), it is clear that an improvement in the angular resolution is only obtained at the expense of determining higher coefficients in the series. However, for a fixed number of coefficients, the image fidelity is here a complex function of the radial position: the image becomes closer to the original distribution whenever only a few coefficients suffice to give a good convergence in the Fourier series.

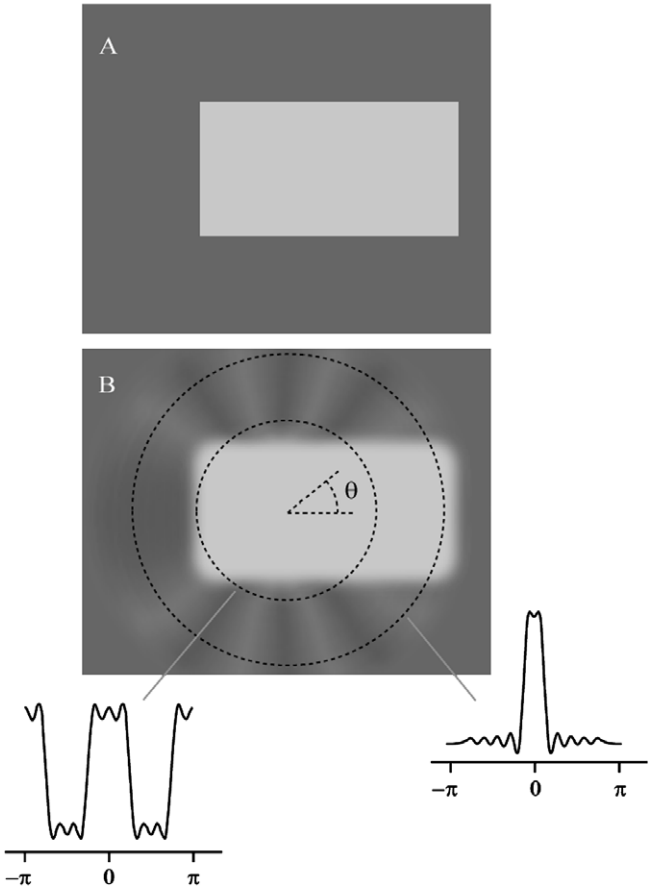

Fig. 7. Phantom (A) and image reconstruction (B) using Scheme 2. The spatial grid had 128×128 square voxels. Despite the simplicity of the spin distribution, one should notice the lack of cylindrical symmetry and the sharp edges of the bar. Two circular cross sections at different radii have been separately represented for clarity. The appearance of oscillations in the vicinity of the edges is induced by the discrete number of Fourier coefficients used (a total of 25 in Formula (13)). Conditions during the simulation were identical to those used in Figs. 4B–D. The separation between pulses was 1 ms.

4. Discussion

The practical implementation of either of the proposed schemes of detection involves a variety of issues difficult to cover in full length. Without trying to exhaust all possibilities, it is possible, nonetheless, to distinguish some outstanding features. For example, regardless of the detection method chosen (such as SQUIDs, optical magnetometry, etc.) sensitivity at very low frequencies is hampered because in this region the $1/f$ noise is dominant [24,25]. In our case, these effects will obviously affect the image quality because the magnitude of the field tends to zero in the central region of the sample. Hence, independently of the chosen scheme, the field of view will in practice be deprived of this central region, where the image will show a bright, featureless disk (similar to the one found for different reasons in Fig. 4B). However, with field gradients of the order of 1 kHz/cm and typical sample sizes, the fraction invisible to the detector is small and, if necessary, can be further reduced by increasing the magnitude of the gradient.

Possibly the most important limitation in Scheme 1 is related to the difficulty in performing a stroboscopic acquisition during a fast train of pulses (particularly if SQUID detection is chosen). This is due to the fact that, in general, the recovery time of the detector is longer than the one found in a tuned circuit at high field. However, it is important to notice that this time can vary several orders of magnitude from several milliseconds to tens of microseconds depending on the used array [26]. In this last case, the range of useful gradients is obviously very large reaching a maximum of almost 10 kHz/cm. Finally, it is worth pointing out that this scheme could be easily altered to monitor the spin evolution in a point-by-point wise fashion. In this incarnation, however, the scheme is not efficient because

the dead time problem is solved at the expense of an extra dimension in the acquisition.

If only for a moment we make aside all practical issues, the fact that Scheme 1 is based on a projection/reconstruction-like approach to recover the sample image represents an intrinsic disadvantage. This is because, as is well known, the sampled points on the reciprocal space are radially distributed and thereby, the image resolution diminishes with the distance to the center. However, it is possible to modify Scheme 1 to make the direction of the pulses change by 90 degrees during the evolution: this would be equivalent to a change in the direction of the gradient in a way similar to the one used in a standard two-dimensional Fourier scheme. In our case, a change in the direction of the effective gradient also creates a change in the direction of the effective field, which makes the situation a bit more complex. However, this is certainly a possibility and has been included for reference in Fig. 4D.

In comparison, Scheme 2 has its own advantages and disadvantages. In this case, for instance, the detector dead time does not represent a relevant problem if the acquisition is initiated at the signal echo *after* preparing the initial state. However, this method has two important problems. In the first place, the relative contribution of each coefficient to the signal decays as the order m increases. This can be clearly observed in the Table in Fig. 6 and is intrinsic to the way chosen here to generate the signal. (This effect could, in principle, be mitigated if all the echoes following the preparation pulses are also considered when recovering the series coefficients. This, however, is not simple and has been avoided here.) The second disadvantage is the fact that the coefficients are determined in an iterative way: the value of $c_m(r)$ is obtained by combining the m-th signal and (several of) the m-1 smaller coefficients. Such a situation is not desirable because the error increases (almost) linearly with the order of the coefficient. In practice, this last problem could be solved by a phase cycling on the preparation pulses to filter out from the signal all coefficients but the one desired. This, however, has not been studied in this manuscript and should be the subject of further analysis in the future.

As a final comment, it is worth noting that both schemes could be extended to three dimensions with relatively minor changes if, for instance, the saddle coil is replaced by an anti-Helmholtz array. In Scheme 1, the elimination of this new field component during each projection would be carried out at the expense of an increase in the pulse density of the train (and a cycling of the pulsing direction). In Scheme 2, the preparation pulses could be selected to determine a spin distribution now expressed as a series of spherical harmonics.

As mentioned in the introduction, there are several reasons that render low magnetic field imaging an attractive research subject. The schemes shown above demonstrate that, contrary to what one could expect, it is indeed possible to reconstruct the spatial distribution of nuclear magnetization, whose evolution takes place in a non-uniform magnetic field with zero average value. In general, this idea can be implemented in multiple different ways although here we have specifically considered two schemes. In the first one, we use a pulse train that, on average, alters the symmetry of the gradient field allowing a spatial encoding similar to standard methods in high fields. In the second scheme, the spatial distribution of the spin system is described by a Fourier series and the initial state of the sample is prepared so that the resulting signal provides information relative to the coefficients of this expansion.

Within the various possible frames of very-low-field detection, our strategy could be of interest because the absence of a more intense homogeneous field eliminates the restrictions on the amplitude of the gradient used to encode the spin positions (i.e., it turns the 'concomitant gradient problem' obsolete). In principle, such a situation could be advantageous because it translates into an increment of the finally attainable resolution for situations in which, due to different reasons, the magnitude of the magnetic field must be small at all sites. Reduction to practice is challenging mainly due to limitations in the currently available hardware. Preliminary experimental results, however, have been reported [27] and will certainly be the subject of future publications elsewhere.

Acknowledgments

We gratefully acknowledge the help, advice, and guidance of Alex Pines. During the early stages of this work, we had helpful discussions with Ms. A. Agrawal.

References

[1] P. Callaghan, Principles of Nuclear Magnetic Resonance Microscopy, University Press, Oxford, 1991.
[2] D.G. Norris, J.M.S. Hutchinson, Concomitant magnetic field gradients and their effects on imaging at low magnetic field strengths, Magn. Reson. Imaging 8 (1990) 33.
[3] M.A. Bernstein, X.H.J. Zhou, J.A. Polzin, K.F. King, A. Ganin, N.J. Pelc, G.H. Glover, Concomitant gradient terms in phase contrast MR: analysis and correction, Magn. Reson. Med. 39 (1998) 300.
[4] C.H. Tseng, G.P. Wong, V.R. Pomeroy, R.W. Mair, D.P. Hinton, D. Hoffmann, R.E. Stoner, F.W. Hersman, D.G. Cory, R.L. Walsworth, Low-field MRI of laser polarized noble gas, Phys. Rev. Lett. 81 (1998) 3785.
[5] P. Morgan, S. Conolly, G. Scott, A. Macovski, A readout magnet for prepolarized MRI, Magn. Reson. Med. 36 (1996) 527.
[6] W.J. Shao, G.D. Wang, R. Fuzesy, E.W. Hughes, B.A. Chronik, G.C. Scott, S.M. Conolly, A. Macovski, Low readout magnetic resonance imaging of hyperpolarized xenon and water in a single system, Appl. Phys. Lett. 80 (2002) 2032.
[7] G.P. Wong, C.H. Tseng, V.R. Pomeroy, R.W. Mair, D.P. Hinton, D. Hoffmann, R.E. Stoner, F.W. Hersman, D.G. Cory, R.L. Walsworth, A system for low field imaging of laser-polarized noble gas, J. Magn. Reson. 141 (1999) 217.
[8] A. Wong-Foy, S. Saxena, A.J. Moulé, H.M.L. Bitter, J.A. Seeley, R. McDermott, J. Clarke, A. Pines, Laser-polarized Xe-129 NMR and MRI at ultra-low magnetic fields, J. Magn. Reson. 157 (2002) 235.
[9] A.K. Venkatesh, A.X. Zhang, J. Mansour, L. Kubatina, C.H. Oh, G. Blashe, M.S. Unlu, D. Balamore, F.A. Jolesz, B.B. Goldberg, M.S.

Albert, MRI of the lung gas-space at very low-field using hyperpolarized noble gases, Magn. Reson. Imaging 21 (2003) 773.
[10] R.W. Mair, M.I. Hrovat, S. Patz, M.S. Rosen, I.C. Ruset, G.P. Topulos, L.L. Tsai, J.P. Butler, F.W. Hersman, R.L. Walsworth, Orientation-dependent ^{3}He lung imaging in an open access very-low-field human MRI system, Magn. Reson. Med. 53 (2005) 745.
[11] R. McDermott, A.H. Trabesinger, M. Muck, E.L. Hahn, A. Pines, J. Clarke, Liquid-state NMR and scalar couplings in microtesla magnetic fields, Science 295 (2002) 2247.
[12] A.H. Trabesinger, R. McDermott, S.K. Lee, M. Muck, J. Clarke, A. Pines, SQUID-detected liquid state NMR in microtesla fields, J. Phys. Chem. A 108 (2004) 957.
[13] R. McDermott, S.-K. Lee, B. ten Haken, A.H. Trabesinger, A. Pines, J. Clarke, Microtesla MRI with a superconducting quantum interference device, PNAS 101 (2004) 7857–7861.
[14] R. McDermott, N. Kelso, S. Lee, M. Mossle, M. Muck, W. Myers, B. ten Haken, H.C. Seton, A.H. Trabesinger, A. Pines, J. Clarke, SQUID-detected magnetic resonance imaging in microtesla magnetic fields, J. Low Temp. Phys. 135 (2004) 793.
[15] S. Lee, M. Moessle, W. Myers, N. Kelso, A.H. Trabesinger, A. Pines, J. Clarke, SQUID-detected MRI at 132 mu-T with T1 contrast weighted at 10 mu-T–300 mT, Magn. Reson. Med. 53 (2005) 9.
[16] M. Moessle, W.R. Myers, S.-K. Lee, N. Kelso, M. Hatridge, A. Pines, J. Clarke, SQUID-detected in vivo MRI at microtesla magnetic fields, IEEE Trans. Appl. Supercond. 15 (2006) 757.
[17] I.M. Savukov, M.V. Romalis, NMR detection with an atomic magnetometer, Phys. Rev. Lett. 94 (2005) 123001.
[18] C.A. Meriles, D. Sakellariou, A.H. Trabesinger, V. Demas, A. Pines, Zero- to low-field MRI with averaging of concomitant gradient fields, PNAS 102 (2005) 1840.
[19] P.A. Bottomley, A versatile magnetic field gradient control system for NMR imaging, J. Phys. E Sci. Instrum. 14 (1981) 1081.
[20] W.E. Maas, F. Laukien, D.G. Cory, Coherence selection by radio-frequency gradients, J. Magn. Reson. A 103 (1993) 115.
[21] D. Canet, P. Tekely, N. Mahieu, D. Boudot, Averaging effects in NMR spectroscopy by a radio-frequency field gradient: induced coherence transfers, Chem. Phys. Lett. 182 (1991) 541.
[22] U. Haeberlen, High-Resolution NMR in Solids. Selective Averaging, Academic Press, New York, 1976.
[23] R.R. Ernst, Principles of Nuclear Magnetic Resonance in One and Two Dimensions, Clarendon Press, Oxford, 1994.
[24] J. Clarke, G. Hawkins, Flicker 1/f noise in Josephson tunnel junctions, Phys. Rev. B 14 (1976) 2826.
[25] C.D. Tesche, J. Clarke, DC SQUID: noise and optimization, J. Low Temp. Phys. 29 (1977) 301.
[26] D.M. TonThat, M. Ziegeweid, Y.Q. Song, E.J. Munson, S. Appelt, A. Pines, J. Clarke, SQUID detected NMR of laser-polarized xenon at 4.2 K and at frequencies down to 200 Hz, Chem. Phys. Lett. 272 (1997) 245.
[27] N. Kelso, S.-K. Lee, L. Bouchard, V. Demas, A. Pines, J. Clarke, SQUID-detected magnetic resonance imaging in zero static magnetic field, March Meeting of the American Physical Society, Baltimore, March 2006.